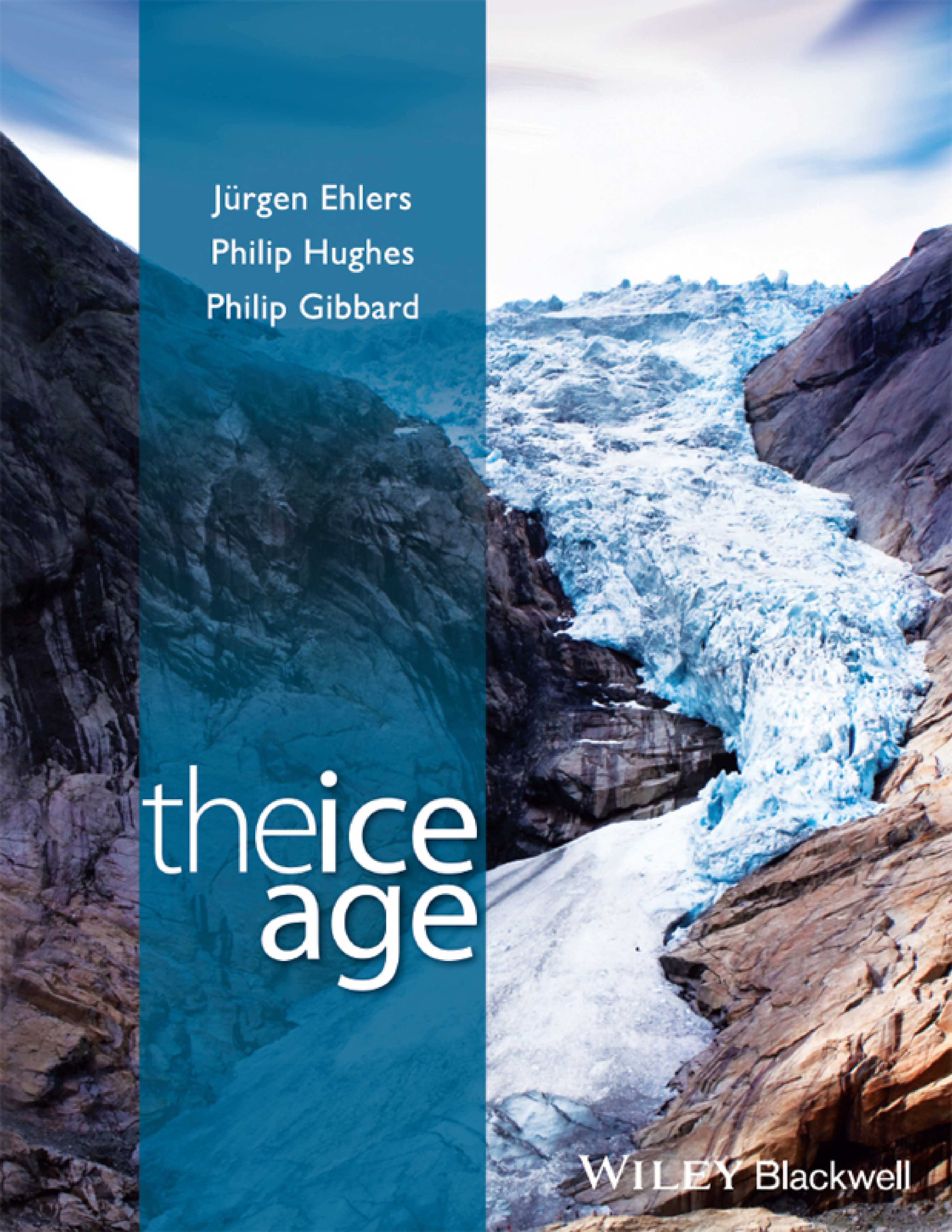

Jürgen Ehlers
Philip Hughes
Philip Gibbard

the ice age

WILEY Blackwell

The Ice Age

Jürgen Ehlers
Witzeeze, Germany

Philip D. Hughes
Reader in Physical Geography, School of Environment, Education & Development, The University of Manchester, Manchester, United Kingdom

Philip L. Gibbard
Department of Geography, University of Cambridge, Cambridge, United Kingdom

WILEY Blackwell

This edition first published 2016 @ 2016 by John Wiley & Sons, Ltd.

Translation from German language edition: *Das Eiszeitalter* by Jürgen Ehlers. Copyright @ Springer Spektrum | Springer-Verlag GmbH 2011 (formerly Spektrum Akademischer Verlag). Springer Spektrum | Springer-Verlag GmbH is a part of Springer Science+Business Media. All Rights Reserved.

Registered office: John Wiley & Sons, Ltd, The Atrium, Southern Gate, Chichester, West Sussex, PO19 8SQ, UK

Editorial offices: 9600 Garsington Road, Oxford, OX4 2DQ, UK
The Atrium, Southern Gate, Chichester, West Sussex, PO19 8SQ, UK
111 River Street, Hoboken, NJ 07030-5774, USA

For details of our global editorial offices, for customer services and for information about how to apply for permission to reuse the copyright material in this book please see our website at www.wiley.com/wiley-blackwell.

The right of the author to be identified as the author of this work has been asserted in accordance with the UK Copyright, Designs and Patents Act 1988.

All rights reserved. No part of this publication may be reproduced, stored in a retrieval system, or transmitted, in any form or by any means, electronic, mechanical, photocopying, recording or otherwise, except as permitted by the UK Copyright, Designs and Patents Act 1988, without the prior permission of the publisher.

Designations used by companies to distinguish their products are often claimed as trademarks. All brand names and product names used in this book are trade names, service marks, trademarks or registered trademarks of their respective owners. The publisher is not associated with any product or vendor mentioned in this book.

Limit of Liability/Disclaimer of Warranty: While the publisher and author(s) have used their best efforts in preparing this book, they make no representations or warranties with respect to the accuracy or completeness of the contents of this book and specifically disclaim any implied warranties of merchantability or fitness for a particular purpose. It is sold on the understanding that the publisher is not engaged in rendering professional services and neither the publisher nor the author shall be liable for damages arising herefrom. If professional advice or other expert assistance is required, the services of a competent professional should be sought.

Library of Congress Cataloging-in-Publication Data

Ehlers, Jürgen, 1948-
[Eiszeitalter. English]
The Ice Age / Jürgen Ehlers, Philip Hughes. and Philip Gibbard.
pages cm
Translated from German: Das Eiszeitalter / by Jürgen Ehlers (Springer-Verlag, GmbH, 2011).
Includes bibliographical references and index.
ISBN 978-1-118-50781-0 (cloth) – ISBN 978-1-118-50780-3 (pbk.) 1. Glacial

epoch.
2. Climatic changes. 3. Glaciology. 4. Glacial landforms. 5. Eolian processes. 6. Ice sheets.
I. Hughes, Philip D. II. Gibbard, Philip L. (Philip Leonard), 1949- III. Title.
QE697.E4413 2015
551.7'92–Cdc23

2015015483

A catalogue record for this book is available from the British Library.

Cover image: Briksdalsbreen Glacier in Jostedalsbreen, Norway @ Getty Images

Contents

List of Tables

List of Illustrations

Figure 1.2 Stranded ice floe with a thick layer of frozen-on soil in the St Lawrence Estuary, Canada. Photograph by Jean-Claude Dionne.

Figure 1.3 View from Gornergrat to Monte Rosa, Switzerland. Above: as seen by Agassiz (source: Agassiz 1841), below: 1979 (photograph by Jürgen Ehlers). The perspective is slightly different, but the decline of the ice on the opposite slope is clearly visible.

Figure 1.4 The lower end of the Gorner glacier (formerly called the Zermatt glacier). Neither of the two ladies at the foot of the glacier or the gentlemen on the adjacent rocks (left) seem to have work to do here; they are probably tourists. Source: Agassiz (1841).

Figure 1.5 An excursion onto the Glacier de Courbassière, Valais, Switzerland. The nineteenth century saw a strong growth in tourism in Switzerland. The wild nature and the glaciers were not only major tourist attractions, but had also become more accessible for scientific research. From the point where the postcard was taken, the glacier seems almost unchanged today. In truth, its length has shrunk by 800 m since 1889.

Figure 1.6 Slab of Rhät sandstone from Velpke (10 km ESE of Wolfsburg, Germany) with striae pointing in two different directions. The slab is located in the Museum of the BGR in Spandau. Photograph by Klaus Steuerwald.

Figure 1.7 Geikie’s map showing the extent of the glaciers of the ‘Third Glacial Epoch’ (i.e. Weichselian) in Europe. The southern boundary of the glaciated area is nearly identical with the present state of knowledge. Source: Geikie (1894).

Figure 1.8 Letter in which Geikie thanks Professor Boule. Albert Faslan, mentioned in the letter, was a French natural scientist who had mapped the erratics in the Rhône catchment area. Source: Faslan & Chantre (1877/78).

Figure 1.9 The Wonders of the Primeval World, by Dr W.E.A. Zimmermann. Source: Zimmermann (1885).

Figure 1.10 Antediluvian man. The author makes fun of the artist who dares to publish ‘an image of our antediluvian ancestors’, but reprints it all the same. Source: Zimmermann (1885).

Figure 1.11 Geological timescale and the occurrence of ice ages in the Earth’s history.

Figure 1.12 Neoproterozoic Moelv Tillite at Moelv, Lake Mjøsa, Norway. Above: overview; below: detail. Photographs by Jürgen Ehlers.

Figure 1.13 Neoproterozoic tillite of the Varanger glaciation at Bigganjarga, Karlebotn, Varanger Peninsula, northern Norway. The tillite is part of the Smalfjord Formation, presumably upper Vendian (Varangerian) in age (>640 Ma). Photograph by Juha-Pekka Lunkka.

Figure 1.14 Neoproterozoic Port Askaig Tillite at the Port Askaig ferry terminal, Isle of Islay, Scotland. Photograph by Jürgen Ehlers.

Figure 1.15 The variations of the orbital parameters: (a) precession; (b) tilt of the Earth’s axis; and (c) eccentricity.

Chapter 2

Stadial 3 is indicated by the dashed lines, and Hughes & Gibbard (2014) argued that this interval best represents the global Last Glacial Maximum (*c.* 25,000 years ago) when global ice volume was at its greatest and global sea levels were at their lowest.

Figure 2.5 Close-up of the Last Glacial Maximum during the time interval 30–20 ka, showing the ice core records from Greenland (NGRIP) and Antarctica (EPICA). The top two diagrams are the oxygen isotope (Andersen et al. 2006) and dust concentration (Ruth et al. 2007) records from the NGRIP core. The NGRIP core is on the GICC05 age model. The bottom two diagrams are the dust flux (Lambert et al. 2012) and deuterium-derived temperature (Jouzel et al. 2007) records from EPICA, Antarctica. The EPICA records are both on the EDC3 age model. H2 and H3 are Heinrich Events when large icebergs were discharged into the North Atlantic Ocean.

Figure 2.6 Glaciation and sea ice during the Weichselian (last) glacial maximum in the Northern and Southern hemispheres.

Figure 2.7 Ice-age glaciations in (a) Europe. (b) North America (c) South America, Africa, Asia and Australia. Purple squares: glacial deposits; ?: questionable glacial deposits; ~ glaciomarine deposits; MIS: Marine Isotope Stage.

Figure 2.8 The extent of the Alpine glaciations.

Figure 2.9 The Thalgut exposure in the Aare valley (south of Bern, Switzerland). In the upper part of the exposure: Rotachewald Diamicton above the Upper Münsingen Gravels. Photograph by Christian Schlüchter.

Figure 2.19 The extent of the Saalian Glaciation in northern Germany.

Figure 2.20 Eemian peat on the banks of the Elbe at Lauenburg. Photograph by Jürgen Ehlers.

Figure 2.21 The original limit of the Weichselian Glaciation (white line, mapped by Gripp 1924) compared to the present-day Weichselian limit (red line, Ehlers et al. 2011a). A = ‘Altmoräne’ (‘Old Morainic’ landscape), J = ‘Jungmoräne’ (‘Young Morainic’ landscape).

Figure 2.22 The extent of the Weichselian Glaciation in northern Germany.

Figure 2.23 Weichselian ice margin in Jutland. The Weichselian glacial area is dissected by numerous subglacial meltwater channels (tunnel valleys), while the older morainic areas and outwash plains, beyond the ice limit, have a smoothed relief and relate to the Saalian Glaciation.

Figure 2.24 Block-strewn Pomeranian Phase end moraine, south of Neubrandenburg. Photograph by Jürgen Ehlers.

Figure 2.25 A boulder being sampled for dating on a moraine in the High Atlas, Morocco. Around 500 g of sample from the top 5 cm thickness was taken from the top of the boulders (which are andesites that contain quartz veins and phenocrysts) for ^{10}Be exposure dating. The mass of sample that is required depends on how much quartz is present, the duration of surface exposure and the altitude/latitude of the site. After extensive treatment in the laboratory *c.* 10–50 g of pure quartz grains were normally required from the High Atlas in order for ^{10}Be to be successfully measured in Late Pleistocene samples. Photograph by Phil Hughes.

Figure 2.26 Locations mentioned in the description of the British glacial succession.

Figure 2.27 The limits of glaciations in the British Isles, representing maximum extent limits. However, the maximum extent lines are known to be diachronous and in some areas these lines are simplifications. For example, for the Devensian limits compare the limits in SW England with those in Figure 2.28 and 2.29.

Figure 2.28 The timing of retreat from the maximum phase of the Late Devensian Ice Sheet over the British Isles and Ireland. Some areas saw earlier retreats from more extensive Devensian positions (see Fig. 2.29).

Figure 2.29 Devensian glaciation in the southern Irish Sea region. The Lundy data are from Rolfe et al. (2012). LGM position and ice directional indicators are based on Ó Cofaigh & Evans (2007, their fig. 2).

Figure 2.30 Extent of ancient glaciations in North America in the: (a) Gauss Chron; (b) lower Matuyama Chron; (c) upper Matuyama Chron; and (d) Brunhes Chron. Adapted from Duk-Rodkin & Barendregt (2011). Reproduced with permission of Elsevier.

Figure 2.31 The intercalation of glacial deposits with tephra layers allows the age determination of the glaciations in large parts of North America. In some cases the till is interspersed with tephra. The picture shows till with volcanic bombs on the shore of Yellowstone Lake, Wyoming. Photograph by Jürgen Ehlers.

Figure 3.5 Longitudinal section through a valley glacier. Newly formed ice from the accumulation area of the glacier flows downvalley. The ice formed in the upper part of the glacier ice moves closest to the glacier sole. The formation of ice continuously decreases towards the equilibrium line. In the ablation zone melt processes steadily increase further downhill.

Figure 3.6 Mountain glaciations will leave a number of prominent landforms that are clearly visible in satellite images. These include numerous cirques, many with cirque lakes at the upper end of the valleys, U-shaped valleys and tongue basins, many of which are filled with lakes. This example shows the Wind River Mountains, Wyoming.

Figure 3.7 Tongue basin with adjoining end moraines. Wind River Mountains, Wyoming. Photograph by Jürgen Ehlers.

Figure 3.8 Glacial erosion transforms the V-shaped valleys created by rivers into U-shaped glacial valleys. Example from northern Sweden, north of Tärnaby. Photograph by Jürgen Ehlers.

Figure 3.9 The formerly glaciated valleys of the Alps can be distinguished from unglaciated valleys from the digital terrain model. (a) Cross-sections through four Alpine valleys(b) location of the cross-sections relative to the Würmian ice margin; and (c) location map.

Figure 3.10 Different types of glacier movement: (a) internal deformation U_V; (b) basal sliding U_G; and (c) subglacial deformation U_D.

Figure 3.11 Digital elevation models highlight landforms that cannot be seen in maps or aerial photographs; at the border between North and South Dakota and Minnesota the terrain surface is overprinted by glacial ice advances: (a) SRTM (Shuttle Radar Topography Mission) elevation model (b) interpretation.

Figure 3.12 Glacially sculptured rocky headland in a Norwegian fjord. Photograph by Jürgen Ehlers.

Figure 3.13 Ice-moulded bedrock on the summits of the Rhinog mountains, North Wales. This evidence illustrates that ice over-ran this mountain range from an ice centre to the east (from right to left). However, in nearby mountains less than 2 m of bedrock has been removed, resulting in cosmogenic nuclide inheritence from previous surface exposures (e.g. in the nearby Aran Mountains, Wales; Glasser et al. 2012). It is therefore likely that multiple glaciations are required to remove larger depths of bedrock across wide areas. Photograph by Phil Hughes.

Figure 3.14 Roche moutonnée in the forefield of Nigardsbreen glacier, Norway. Photograph by Jürgen Ehlers.

Figure 3.15 Drumlins and related landforms, Donegal Bay, Ireland. The cross-valley landforms are called *Rogen Moraine*.

Figure 3.16 Wisconsin drumlin swarm in the satellite image.

Figure 3.17 Glacial striae and iron precipitates in the lee of obstacles in the Nigardsbreen glacier forefield, Norway. Photograph by Jürgen Ehlers.

Figure 3.18 Dirt cone on the surface of Kverkjökull, Iceland. Photograph by Jürgen Ehlers.

Figure 3.19 Entrance to an abandoned meltwater tunnel under Nigardsbreen glacier, Norway. Photograph by Jürgen Ehlers.

Figure 3.20 Abandoned meltwater tunnel at the base of Nigardsbreen, Norway. Photograph by Jürgen Ehlers.

Figure 3.21 Volcanic eruption under Vatnajökull, Iceland, October 1996. Photograph by Magnús Tumi Gumundsson.

Figure 3.22 Jökulhlaup in Iceland: icebergs floating in the swirling meltwater. Photograph by Magnús Tumi Gumundsson.

Figure 3.23 The end of the jökulhlaup. Bridges have been destroyed and the ring road is impassable. Photograph by þröstur þorsteinsson.

Chapter 4

Till profile with intercaleted, washed-out large sand lens; Brodtener Ufer cliff at Travemünde, Schleswig-Holstein. Photograph by Jürgen Ehlers.

Figure 4.1 Till on Iceland. The dark colour of the matrix is caused by the reworking of basaltic rocks. Photograph by Jürgen Ehlers.

Figure 4.2 Tillite (lithified till) on Iceland. The glacial striae have been caused by the latest glaciations. Photograph by Jürgen Ehlers.

Figure 4.3 Lodgement till (top) and meltout till (bottom), Langeland, Denmark. The penguin in the bottom image is 12.5 cm high. When were these tills deposited? The geographer Albrecht Penck originally had the view that a layer of glacial debris several metres in thickness might be moved beneath the ice. Based on his investigations in Greenland, Von

Drygalski (1897) came to the conclusion that the morainic material had been transported in the basal portions of the ice. This view prevailed, but today we know that some sediment transport also takes place below the ice. Photographs by Jürgen Ehlers.

Figure 4.4 Earth pillars at Euseigne, Switzerland. Photograph by Jürgen Ehlers.

Figure 4.5 Scarborough Bluffs, Ontario. Morainic deposits (left) and glaciolacustrine silts (right) deposited in a subglacial meltwater channel. Photographs by Adriaan Janszen.

Figure 4.6 Glaciolacustrine clays of a Late Weichselian ice-dammed lake exposed in the construction site for the Travemünde ferry terminal (near Lübeck, Germany). Photograph by Jürgen Ehlers.

Figure 4.7 Till types from North Germany: (a) sandy Elsterian till from Wellen, Lower Saxony; (b) clay-rich Middle Saalian till from Grauen, Lower Saxony; and (c) red Younger Saalian till (Vastorf Till) from Emmendorf, Lower Saxony. Photographs by Jürgen Ehlers.

Figure 4.8 Alpine till with striated clast. Photograph by Jürgen Ehlers.

Figure 4.9 Fine-grained matrix-supported till containing erratic cobble clasts at Thursaston, Wirral peninsula, NW England. These deposits were formed at the base of the Irish Sea Ice Sheet during the last glaciation. Photograph by Phil Hughes.

Figure 4.10 Till clast composition in relation to changing bedrock conditions in Sweden.

Figure 4.11 (a) Giant erratic 'Alter Schwede' (Old Swede) at the River Elbe near Hamburg and (b) the scar where the core sample was drilled. Photographs by Jürgen Ehlers.

Figure 4.12 Supraglacial and subglacial transport of morainic material by the glacier: (a) rock debris on the surface of Tsijiore Nouve glacier, Switzerland. Photograph by Jürgen Ehlers. (b) Banded, debris-rich ice at the base of Taylor Glacier, Antarctica. Photograph by John Shaw.

Figure 4.13 The Yankee Fork gold dredge, Idaho. Photograph by Jürgen Ehlers.

Figure 4.14 Clast orientation measurements in till and underlying glaciolacustrine deposits on the Isle of Langeland (Denmark). In the lake sediments many stones are upright, and there is no clear orientation of the long axes. Photograph by Jürgen Ehlers.

Figure 4.15 In some cases the deposits of different ice advances can be distinguished based on their clast orientation. Till fabric measurements from three tills from the Hamburg region in Germany: (a) Older Saalian advance (b) Middle Saalian advance; and (c) Younger Saalian advance.

Figure 4.16 (a) Volcanic erratic boulder in the old Quadrangle at the University of Manchester. This boulder has a source over a hundred kilometres away in the English Lake District. (b) Text on a plinth adjacent to the erratic. Photographs by Phil Hughes.

Figure 4.17 Shap Granite erratics have spread widely from their original area. In this example, a granite boulder rests on limestone bedrock in the NW Pennines, England. Photograph by Phil Hughes.

Figure 4.18 Crystalline Scandinavian indicator clasts: (a) Rhomb Porphyry; (b) Red Baltic Porphyry; (c) Åland Rapakivi; (d) typical quartz grain in an Åland quartz porphyry; (e) Kine Diabase; (f) Västervik Spotted Rock;and (g) Påskallavik Porphyry. Photographs by Jürgen Ehlers.

Figure 4.19 Composition of different grain-size fractions of Elsterian till from a depth of 34–35 m from the Dradenau KB 42 core drilling in Hamburg-Waltershof. The finer the material, the higher the quartz content.

Figure 4.20 Fine gravel analyses from till samples from Ristinge Klint, Langeland, Denmark: (a) limestones; and (b) non-limestones. The three tills can be clearly distinguished. (The raft of reddish till found in the western part of the section is strikingly different from the rest of the samples.)

Figure 4.21 QEMSCAN analyses of till samples from Hamburg, Germany: (a) quartz; (b) biotite; (c) muscovite; (d) dolomite (continued) (i) tourmaline; (j) epidote; (k) glauconite; (l) illite (continued) (m) smectite; (n) chlorite; and (o) kaolinite.

Figure 4.22 QEMSCAN analysis general view image used to detect irregularities. In this sample several large grains of dolomite are visible, which account for the irregularity in Figure 4.21d (sample 11).

Figure 4.23 Redeposited Quaternary foraminifera in the tills from Ristinge Klint, Denmark. For comparison: foraminifera from the marine Eemian Græsted Clay of Tulstrup. Adapted from Sjørring et al. (1982). Reproduced with permission of Dansk Geologisk Forening.

advance, the Ristinge Ice Stream, reached Denmark. (b) In the subsequent Main Weichselian Ice Advance, the Baltic Sea Basin played no role in controlling the ice movement.(c) During the Young Baltic Advance, ice movement was again controlled by the Baltic Sea Basin. (d) The last ice advance, the Bælthav Advance, brought rock material from more easterly source areas to Denmark.

Chapter 5

Giant pothole in the forefield of Briksdalsbreen glacier, Norway. Photograph by Jürgen Ehlers.

Figure 5.1 Fjords in Alaska in the satellite image. In the low-lying parts, former cirques can be seen which became ‘drowned’ in the postglacial sea-level rise. The narrow ridges between those cirques are called arêtes.

Figure 5.2 The Sognefjord is 204 km long and, at the lowest point, the bedrock lies about 1500 m below the water table. Photograph by Jürgen Ehlers.

Figure 5.3 Lake Schmalsee, a subglacial meltwater erosion channel north of the Weichselian ice margin near Mölln, Schleswig-Holstein. Photograph by Jürgen Ehlers.

Figure 5.4 Fifteen generations of Pleistocene subglacial channels at the bottom of the North Sea. The channels are completely filled with sediment and only visible in the 3D seismic data. In the section shown there are two underground salt domes (SD), and the channels run around the salt domes.

Figure 5.5 Detailed view of two glacial meltwater channels on the North Sea floor as depicted in 3D seismic data. The irregular base typical for subglacial channels is clearly visible in both channels.

Figure 5.6 Resistance measurements can be used to explore the subsurface geology and to detect buried channels. Here the EM-31 device of the Canadian Geonics company is seen in operation. Photograph by Steve Mathers.

Figure 5.7 Small Elsterian channels in East Anglia, UK, discovered by resistance measurements. Above: the course of the channels; bottom: resistivity profile and cross-section based on boreholes at Snape Hall, Suffolk.

Figure 5.8 Traces of meltwater erosion at Hillington, Norfolk, UK. The upper part of the chalk has been incorporated in the glacier movement, and plucking has resulted in the formation of steps. Meltwater sand has been washed into the clefts of the highly fractured chalk. Ice movement was from left to right.

Figure 5.9 Sand grains under the electron microscope. (1–6) Till from the Oslo Fjord area, Norway and (7–13) till from Hamburg. The sand grains from Norway show fresh fractures; the grains from Hamburg traces of strong weathering. Photographs by Jürgen Ehlers.

Figure 5.10 (a) Eskers at Folldal, Norway. (b) Exposure in an esker at Folldal, Norway. The coarse, well-rounded pebbles of these eskers, the ‘Rolling Stones’, provided the starting point for the discussion of the great stone flood. Photographs by Jürgen Ehlers.

Figure 5.11 Skeiðará-Sandur, outwash plain at the southern edge of Vatnajökull in Iceland, with the typical braided drainage system. Photograph by Jürgen Ehlers.

Figure 5.12 Sandur sediments at the edge of Kverkjökull glacier in Iceland. Photograph by Jürgen Ehlers.

Figure 5.13 Flow directions (a) on the Skeiðará-Sandur, Iceland, and (b–d) in the Harburger Berge hills near Hamburg. The wide range of drainage directions is typical of a braided river system.

Figure 5.14 Drainage directions of the Saalian meltwater streams in the Hamburg area. (a) Middle Saalian Glaciation (older phase): The ice is coming from the NE and drainage to the NW is still open. (b) Middle Saalian Glaciation (younger phase): the ice margin has advanced and the runoff is now directed to the SW towards the Weser. (c) Younger Saalian Gaciation: the ice is coming from the east and the drainage through the Elbe Valley is free.

Figure 5.15 Deposits of Lake Agassiz, an ice-dammed lake in North America. (a) False-colour satellite image; the stripes are giant striae produced by icebergs.

Figure 5.16 Seasonally layered lake sediments from Lake Sacrow near Potsdam, Germany. Centre: photograph of the carbonate-organic varves of a frozen core. The light layers represent summer calcite precipitate. Right: radiograph of the same frozen core. The calcite precipitates are the clearly visible dark layers. Left: micrograph of varves from Lake Sacrow under polarized light, revealing the internal structure of the annual layers. In most cases three sublayers are recognizable: most notably is the white summer calcite layer. It is overlain by the grey detritus layer of autumn/winter. Below the calcite layer (and not always well developed) is a relatively dark spring layer of diatoms. Photographs by Bernd Zolitschka.

Figure 5.17 Varve thickness measurements of four parallel sedimentary sequences from Holzmaar lake, Westeifel volcanic field. Counts and thickness measurements by B. Zolitschka (HTM-B/C) and B. Rein (HTM-1, HTM 2, HTM-3) were performed on thin sections of the early Holocene varve sequence. The average of the four determinations is shown in the upper graph (red) together with a moving average over seven points (blue). These curves show the Holzmaar system's response to the early Holocene Preboreal (11,400–11,000 cal BP) and Boreal (10,500–10,200 cal BP) climatic oscillations. Both climate fluctuations resulted in thicker varves, caused by increased minerogenic sediment entry.

Figure 5.18 Grimsmoen, a delta of a Weichselian ice-dammed lake in Folldal, Norway. Photograph by Jürgen Ehlers.

Figure 5.19 Deposits of ice-dammed lakes: varves overlying Saalian till in Neumark-Nord opencast mine (left); varved silt in Sweden (right). Photographs by Jürgen Ehlers.

Figure 5.20 Moulin kame on Langeland, Denmark. The gravel hill was accumulated in a glacier mill during the Weichselian Glaciation. Photograph by Jürgen Ehlers.

Figure 5.21 Two examples of *hatbakker*, the so-called 'hat-shaped hills' on Langeland. These are kames which were created in the decay phase of the Weichselian ice age. Photograph by Jürgen Ehlers.

Figure 5.22 (a) Cliff sections through *hatbakker* on the Danish island of Langeland; (b) cross-sections through the Dovns Klint and Bagenkopsbjerg *hatbakker*; and (c) photograph from Bagenkopsbjerg. (a, c) Photographs by Jürgen Ehlers.

Figure 5.23 Kame terrace at Loch Etive, Scotland: (a) kame terrace surface with dead-ice hollow; and (b) the kame terrace deposits. Photographs by Jürgen Ehlers.

Figure 5.24 Kame at Groß Zecher, Schaalsee Lake, Schleswig-Holstein. Photograph by Jürgen Ehlers.

Figure 5.25 Kryižu kalnas (Hill of the Crosses) at Šiauliai in Lithuania is also a kame. Photograph by Jürgen Ehlers.

Figure 5.26 The traces of the Missoula Flood are clearly evident in the Channeled Scablands in Washington State.

Figure 5.27 Erratic block beyond the limits of glaciation in Idaho, the result of a meltwater flood from the outbreak of an ice-dammed lake. Photograph by Jürgen Ehlers.

Figure 5.28 Gravel dunes in the Todza Basin, Altai, which are traces of a catastrophic outflow of an ice-dammed lake. Note the car for scale. Photograph by Keenan Lee.

Figure 5.29 Development of the *urstromtal* drainage in the Weichselian Glaciation. (a) Glogau–Baruth *urstromtal*; (b) Warsaw–Berlin *urstromtal*; (c) drainage shifting to the north. (d) Thorn–Eberswalde *urstromtal*; and (e) relocation of the drainage to the edge of the present Baltic Sea.

Figure 5.30 Thorn–Eberswalde *urstromtal*(white arrows) branching off from the Vistula (Weichsel) river valley near Bydgoszcz in Poland. The ragged

Chapter 6